Chemical Engineering Journal 546 (2026) 180509

Contents lists available at ScienceDirect

Chemical Engineering Journal

journal homepage: www.elsevier.com/locate/cej

Defect-engineered Cu_2O/g-C_3N_4 for enhanced catalytic ozonation via surface hydroxyl enrichment and nitrogen-vacancy-guided interfacial construction

Mingyue Li [a,b,c], Zhuang Guo [b,c,*], Zhixiong Hu [b,c], Dan Li [b,c], Fang Chang [d], Jian Wei [b,c], Maosheng Zheng [a,*]

[a] Key Laboratory of Resources and Environmental Systems optimisation, Ministry of Education, College of Environmental Science and Engineering, North China Electric Power University, Beijing, 102206, China
[b] State Key Laboratory of Environmental Criteria and Risk Assessment, Chinese Research Academy of Environmental Sciences, Beijing, 100012, China
[c] Institute of Water Eco-environment Research, Chinese Research Academy of Environmental Sciences, Beijing, 100012, China
[d] Marine Resources Research Centre, Tianjin Research Institute for Water Transport Engineering, M.O.T., Tianjin, 300456, China

ARTICLE INFO

Keywords:
Heterogeneous catalytic ozonation
Nitrogen vacancy
Cu_2O/g-C_3N_4
Surface hydroxyl enrichment
Interfacial electron transfer

ABSTRACT

Heterogeneous catalytic ozonation (HCO) is a promising technology for the deep removal of refractory organic pollutants; however, its performance remains constrained by a limited density of active sites, sluggish interfacial electron transfer, and poor stability of active metal species. In this study, a defect–engineered Cu_2O/g-C_3N_4 composite catalyst (denoted as Cu–CN) was fabricated using a supramolecular preassembly–thermal polycondensation strategy. This Cu–CN catalyst featuring highly dispersed Cu_2O nanoclusters anchored within a nitrogen–vacancy–guided interfacial structure was applied to oxalate catalytic ozonation. The optimised Cu–CN/O_3 system achieved over 99% oxalate removal within 15 min, with an apparent rate constant (k_{obs}) of 0.253 min^{-1}, approximately 39 times that of ozonation alone, and an ozone utilization efficiency of approximately 62.1%. Structural characterisation, structure–activity relationships, in situ spectroscopic analyses, and DFT calculations collectively provided evidence for a defect–regulated interfacial activation pathway involving two cooperative processes: surface –OH enrichment promoted the dynamic evolution of hydroxylated interfacial species favourable for O_3 activation, while N_v–mediated anchoring stabilised low–valence Cu_2O nanoclusters and strengthened interfacial electronic coupling with the g-C_3N_4 matrix. Collectively, these features facilitated electron–transfer–driven O_3 activation and sustained generation of reactive oxygen species, thereby enabling efficient oxalate degradation. This study provides a defect–guided interfacial construction strategy for developing efficient and stable carbon–nitride–based catalysts for ozone–driven degradation of refractory organic pollutants.

1. Introduction

Advanced oxidation processes (AOPs) are widely adopted for the treatment of refractory organic pollutants owing to their powerful oxidative capacity and broad applicability [1–3]. However, under practical operating conditions, complex organic compounds are often progressively transformed into low–molecular–weight carboxylic acids, which are difficult to oxidise further. Among these, oxalic acid/oxalate tends to persist in the late stages of oxidation because of its inherently low reactivity toward O_3; it is therefore commonly employed as a model pollutant to evaluate the deep–oxidation capability of catalytic ozonation systems [4,5].

In the treatment of refractory organic pollutants, heterogeneous catalytic ozonation (HCO) has attracted considerable attention as it enhances pollutant degradation while minimising the risk of secondary pollution [6–8]. Supported composite catalysts are widely used in HCO because of their high catalytic activity and key role in determining ozonation efficiency [9–11]. Nevertheless, most existing materials face several persistent challenges, including leaching of active components, insufficient density of intrinsic active sites, and sluggish interfacial electron transfer [12–15]. Accordingly, the development of catalysts that combine high activity with robust stability, together with a clear

* Corresponding authors.
E-mail addresses: guozhuang_ran@163.com (Z. Guo), maoshengzheng@ncepu.edu.cn (M. Zheng).

https://doi.org/10.1016/j.cej.2026.180509
Received 20 May 2026; Received in revised form 25 July 2026; Accepted 8 August 2026
Available online 9 August 2026

mechanistic understanding, remains a central challenge in this field.

To address these challenges, the development of metal–support composites with strong interfacial interactions has emerged as an effective strategy [16,17]. Graphitic carbon nitride (g–C_3N_4), owing to its unique tri–s–triazine framework and abundant nitrogen lone–pair electrons, represents an attractive support platform for anchoring metal species [18–21]. Copper, with its excellent electron–transfer capability and reversible Cu^{+}/Cu^{2+} redox cycling, has shown considerable potential for O_3 activation [22,23]. Although CuO/g–C_3N_4 or Cu_2O/g–C_3N_4 heterojunctions have been studied in photocatalysis, their application in heterogeneous catalytic ozonation remains largely unexplored [24]. In contrast, previous catalytic ozonation studies have mainly focused on CuO/g–C_3N_4 and $CuMn_2O_4$/g–C_3N_4 composites, which involve conventional CuO or mixed–metal–oxide interfaces rather than low–valence Cu_2O [25,26]. Thus, constructing a stable low–valence Cu_2O/g–C_3N_4 interface and clarifying its role in O_3 activation remain important unresolved issues. Previous studies have highlighted that catalytic activity strongly depends on interfacial electronic coupling [27,28]. However, conventional metal–loading strategies remain inadequate for simultaneously promoting interfacial electron transfer and stabilizing active Cu species. Therefore, achieving simultaneous stabilisation of low-valence Cu species and promotion of interfacial electron transfer requires rational regulation of the local defect environment.

Recent studies have increasingly shifted catalyst design from conventional metal loading toward interface engineering, in which local coordination environments, interfacial electronic coupling, and defect–regulated active sites are recognized as key determinants of ozone activation efficiency [29–31]. In particular, nitrogen–vacancy engineering in g–C_3N_4 can modulate the local electronic structure, create preferential metal–anchoring sites, and strengthen metal–support interactions [32–34]. Earlier studies on defective heterostructures have shown that nitrogen vacancies may form vacancy complexes or defect clusters rather than isolated sites, and their catalytic effects are strongly influenced by local lattice arrangement and coordination environment [35]. In this context, N_v engineering may provide a feasible route to stabilize low–valence Cu_2O species on g–C_3N_4 and construct electronically coupled Cu_2O/defective g–C_3N_4 interfaces. Such interfaces may also favour surface –OH enrichment, thereby facilitating O_3 adsorption and activation. Nevertheless, it remains unclear how nitrogen vacancies, low-valence Cu_2O nanoclusters, and dynamically evolving hydroxylated interfacial species cooperatively regulate interfacial electron transfer and ROS generation during catalytic ozonation. This knowledge gap hinders the rational design of defect-engineered catalysts that simultaneously achieve high activity and long-term stability. Consequently, coupling highly dispersed metal anchoring with defect regulation offers a promising route to simultaneously improve catalytic activity and structural stability in HCO catalysts.

Unlike previous studies that separately explored Cu_2O/g–C_3N_4 photocatalysts, CuO/g–C_3N_4 and $CuMn_2O_4$/g–C_3N_4 catalytic ozonation systems, or metal–nitrogen–carbon coordination structures for ozone activation [9,25,36,37], this work integrates nitrogen–vacancy engineering with the construction of a low–valence Cu_2O/g–C_3N_4 interface to simultaneously stabilize active Cu species, strengthen interfacial electronic coupling, and enhance ozone activation [9,26,37,38]. Accordingly, an N_v–guided Cu_2O/defective g–C_3N_4 interface was rationally designed to couple Cu_2O stabilisation, surface –OH enrichment, and accelerated interfacial electron transfer for sustained reactive oxygen species (ROS) generation. A Cu–CN composite catalyst with highly dispersed Cu_2O nanoclusters anchored by nitrogen vacancies was synthesised via a supramolecular preassembly–thermal polycondensation strategy and applied to heterogeneous catalytic ozonation of oxalate. The effects of the calcination temperature on nitrogen–vacancy formation, Cu_2O evolution, catalytic activity, and structure–activity relationships were systematically investigated. Furthermore, the respective contributions of nitrogen–vacancy–related defect structures and hydroxyl–related surface species to ozone activation, together with the dominant ROS involved in oxalate degradation, were investigated through complementary experimental analyses. Finally, by integrating multidimensional characterisation, radical identification, in situ diffuse reflectance Fourier–transform infrared spectroscopy (DRIFTS), and DFT calculations, a cooperative interfacial activation mechanism involving N_v–mediated Cu_2O stabilisation, hydroxyl–related surface species, and interfacial electron transfer was proposed and supported. These findings provide mechanistic insights into the rational design of defect–engineered Cu_2O/g–C_3N_4 interfaces for efficient catalytic ozonation and offer guidance for the development of advanced heterogeneous catalytic ozonation catalysts for water treatment.

2. Materials and methods

2.1. Chemicals

All chemicals, including melamine ($C_3H_6N_6$), cyanuric acid ($C_3H_3N_3O_3$), copper(II) nitrate trihydrate ($Cu(NO_3)_2{\cdot}3H_2O$), ethylene glycol ($C_2H_6O_2$), ethanol (C_2H_5OH), *tert*–butanol (TBA), catalase (CAT), p–benzoquinone (BQ), anhydrous trisodium phosphate (Na_3PO_4), 5,5–dimethyl–1–pyrroline N–oxide (DMPO), sodium oxalate ($Na_2C_2O_4$), sodium hydroxide (NaOH), and nitric acid (HNO_3), were purchased from Shanghai Macklin Biochemical Co., Ltd. (China). NaOH and HNO_3 were used for pH adjustment. All reagents were of analytical grade and were used without further purification. Ultrapure water (resistivity $\geq$18.2 MΩ·cm) was used throughout the experiments.

2.2. Materials preparation

The g–C_3N_4 precursor was synthesised via a supramolecular preassembly method. Equimolar amounts of melamine (1.05 g) and cyanuric acid (1.05 g) were dissolved separately in ethylene glycol. The melamine solution was then added dropwise to the cyanuric acid solution in an oil bath at 105 °C, followed by vigorous stirring for 20 min. After cooling to room temperature, the resulting white precipitate was collected by centrifugation, washed with deionised water and ethanol, and dried at 60 °C for 12 h to yield the supramolecular precursor [38].

Cu–CN composites were synthesised by thermal polycondensation. The as–prepared precursor was ground thoroughly with Cu $(NO_3)_2{\cdot}3H_2O$, transferred to a tube furnace, heated to the target temperature at 5 °C min^{-1} under an N_2 atmosphere, and calcined for 2 h. To optimise the Cu–CN preparation conditions, the calcination temperature was varied from 400 to 550 °C at a fixed Cu dosage of 0.15×10^{-3} mol, followed by varying the Cu dosage from 0.05 to 0.20×10^{-3} mol at 500 °C. The resulting samples were denoted Cu–CN–T and Cu–CN–x, respectively. Cu–CN–500 and Cu–CN–0.15 refer to the same optimised catalyst, hereafter denoted as Cu–CN.

2.3. Materials characterisation

The morphology and elemental distribution of the materials were examined by scanning electron microscopy (SEM), transmission electron microscopy (TEM), and energy–dispersive X–ray spectroscopy (EDS). The crystal structure, surface functional groups, and chemical states were characterized by X–ray diffraction (XRD), Fourier–transform infrared spectroscopy (FTIR), and X–ray photoelectron spectroscopy (XPS), respectively. The specific surface area and pore structure were determined from N_2 adsorption–desorption measurements. The surface charge properties were evaluated by zeta–potential analysis, while the interfacial electron–transfer behaviour was investigated using electrochemical impedance spectroscopy (EIS). N_v–related signals and ROS were detected by electron paramagnetic resonance (EPR) spectroscopy. The bulk Cu contents of the Cu–CN–T catalysts were quantified by X–ray fluorescence (XRF) spectroscopy. Detailed information on the instrument models and testing parameters is provided in the Supporting

Information (Table S1).

2.4. Catalytic ozonation performance evaluation

Catalytic ozonation experiments were conducted in a glass reactor using sodium oxalate as the target pollutant. Typical conditions were as follows: initial sodium oxalate concentration, 100 mg L^{-1}; reaction volume, 250 mL; catalyst dosage, 0.1 g L^{-1}; and reaction temperature, 25 °C. Gaseous O_3 was continuously introduced at an O_3 feed rate of 0.58 mg min^{-1} with a gas flow rate of 100 mL min^{-1}. Unless otherwise stated, the initial solution pH was not adjusted. For pH–dependent experiments, the initial pH was adjusted with dilute HNO_3 or NaOH prior to reaction. Samples were collected at predetermined time intervals, and the sodium oxalate concentration was quantified by HPLC. The dissolved Cu concentration in the reaction solution was determined using ICP–MS to assess catalyst stability. ROS generation was identified by EPR coupled with DMPO spin–trapping. Detailed HPLC, ICP–MS, EPR, and gas–phase O_3 determination procedures are provided in the Supporting Information (Table S1 and Text S2).

2.5. Density functional theory (DFT) calculations

All density functional theory (DFT) calculations were performed using a first–principles approach. Detailed computational methods and parameter settings are provided in the Supporting Information (Text S1).

3. Results and discussion

3.1. Structural and morphological characterisation

Cu–CN composites were prepared using a facile supramolecular preassembly–thermal polycondensation strategy, as shown in Fig. 1a. To examine the influence of calcination temperature on crystal structure, XRD analysis was performed for samples calcined at different temperatures (Fig. 1b). All Cu–CN samples exhibited characteristic diffraction peaks at 12.9° and 27.4°, assigned to the (100) in–plane structural units and (002) interlayer stacking planes of g–C_3N_4, respectively [39]. These results indicate that Cu incorporation and thermal treatment preserved the typical layered framework of g–C_3N_4. Notably, no distinct Cu–related diffraction peaks were observed, indicating that no well–crystallized bulk Cu–containing phase was detectable by conventional powder XRD.

To further determine whether the preserved crystalline framework is accompanied by local bonding and defect evolution, the structural evolution of the framework and surface functional groups of Cu–CN were examined by FTIR spectroscopy. The FTIR spectra in Fig. 1c show that all samples retained the characteristic heptazine–ring breathing vibration at 806.5 cm^{-1} and C—N heterocyclic stretching vibrations at 1240–1640 cm^{-1} [40], confirming the preservation of the g–C_3N_4 framework. With increasing calcination temperature, a distinct C≡N band emerged at 2180 cm^{-1}. This feature is commonly attributed to partial cleavage of C—N bonds in g–C_3N_4 and is widely regarded as a

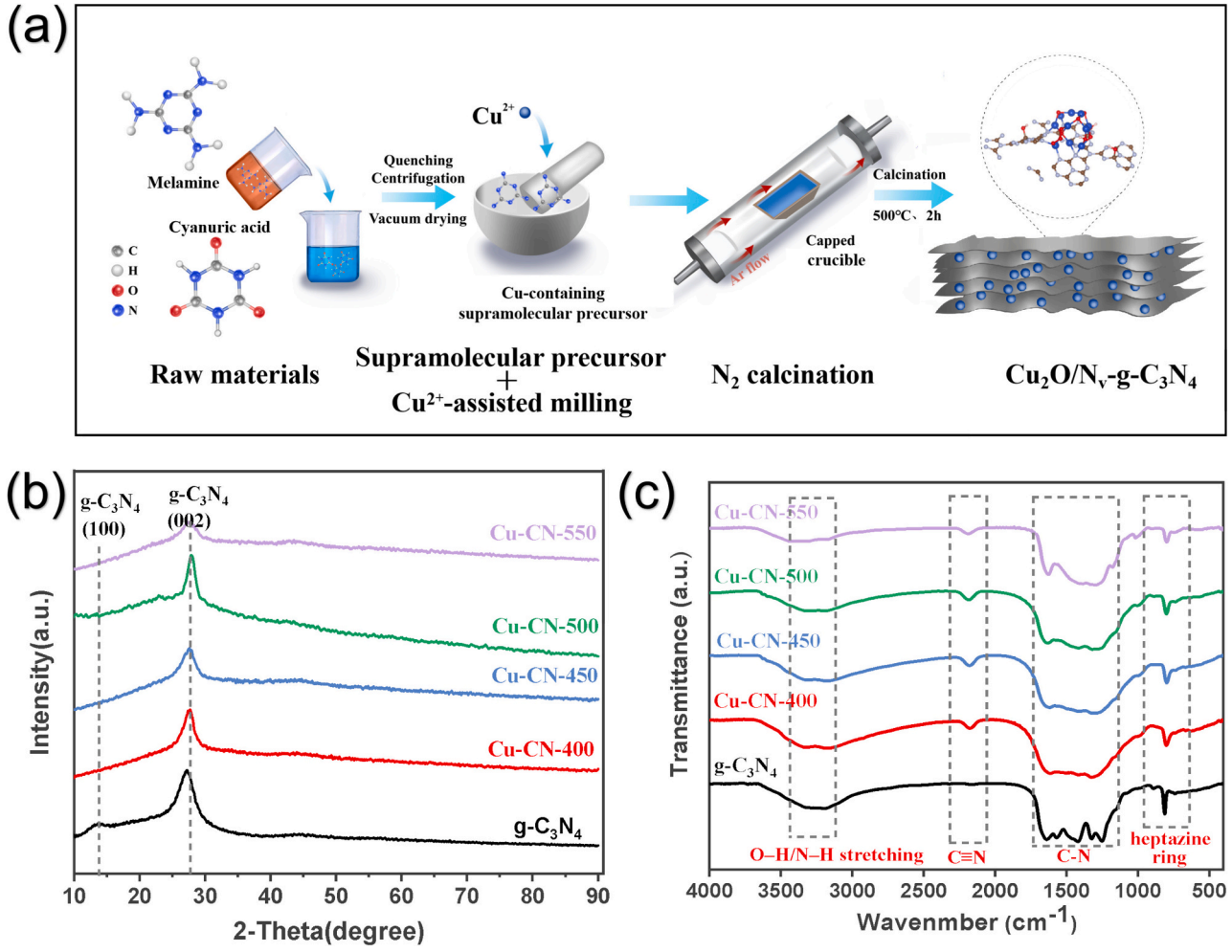

Fig. 1. Synthesis and structural characterisation of Cu–CN composites: (a) schematic illustration of the supramolecular preassembly–thermal polycondensation process; (b) XRD patterns; and (c) FTIR spectra of pristine g–C_3N_4 and Cu–CN samples calcined at different temperatures.

structural signature of N_v formation [41,42]. This observation should be interpreted together with the subsequent XPS and EPR analyses. Further, an enhanced broad band was observed at 3000–3700 cm^{-1}, which was assigned to O–H/N–H stretching vibrations, indicating an increased abundance of hydrogen–containing surface groups and/or contributions from adsorbed water [43,44]. Therefore, while XRD confirms the retention of the long–range g–C_3N_4 framework, FTIR reveals temperature–dependent local structural and surface chemical evolution. In addition, N_2 adsorption–desorption measurements (Fig. S1) confirmed that the samples possess mesoporous structures [45]. Brunauer–Emmett–Teller (BET) analysis (Table S2) showed that the optimised Cu–CN exhibited a specific surface area of 52.45 m^2 g^{-1}, approximately twice that of pristine g–C_3N_4 (27.48 m^2 g^{-1}), which may facilitate mass transfer and expose more accessible interfacial sites. However, the increased surface area alone cannot fully explain the catalytic behaviour, because catalytic ozonation is also strongly influenced by surface chemistry, defect structures, metal active sites, and interfacial electron transfer [14], as examined in the following sections.

Guided by the XRD and FTIR results, which suggest preserved CN framework features and highly dispersed Cu species, the morphology and nanoscale distribution of Cu were further examined by electron microscopy. TEM images (Fig. 2a) and SEM images (Fig. S2) reveal that Cu–CN comprises interwoven, wrinkled two–dimensional nanosheets, forming an open porous architecture without apparent aggregation of large metal particles. The SAED pattern (inset of Fig. 2a) exhibits diffused diffraction rings, indicating the low crystallinity of the matrix, consistent with the XRD results. HRTEM analysis (Fig. 2b) reveals a well–ordered Cu–containing nanocrystalline domain with an interplanar spacing of approximately 0.246 nm, and the corresponding fast Fourier transform (FFT) pattern obtained from the marked region exhibited two non–collinear diffraction spots indexed to the (1–$\bar{1}$–$\bar{1}$) and (00–$\bar{2}$) reflections of cubic Cu_2O. Together with the Cu 2p XPS and Cu LMM Auger electron spectroscopy (AES) analyses, the indexed FFT pattern provides further evidence for the formation of highly dispersed Cu_2O nanocrystalline domains on the g–C_3N_4 matrix. High–angle annular dark–field scanning transmission electron microscopy (HAADF–STEM) and EDS elemental mappings (Fig. 2c–f) show that C and N uniformly define the nanosheet framework, whereas Cu signals are sparse but homogeneously distributed throughout, indicating that Cu species are well dispersed and anchored on the g–C_3N_4 substrate without detectable aggregation. These observations confirm the formation of a dispersed Cu_2O/g–C_3N_4 interfacial structure rather than separated bulk Cu oxide particles.

After confirming the morphology and nanoscale dispersion of Cu species, XPS was subsequently employed to elucidate the surface elemental composition, chemical states, and defect characteristics of Cu–CN. The XPS survey spectrum (Fig. S3) confirmed the presence of C, N, O, and Cu. The high–resolution N 1 s spectrum (Fig. S4a) was deconvoluted into three components at 398.6, 400.5, and 404.4 eV, assigned to pyridinic N (N_2C), pyrrolic/tertiary N (N_3C), and amino N (–NHx), respectively [46,47]. With increasing calcination temperature, the N_3C/N_2C peak–area ratio decreased markedly (Table S3), indicating the loss of three–coordinated N sites during thermal treatment and providing indirect evidence for N_v formation [48–50]. Consistently, the C 1 s spectra (Fig. 3a) show that, in addition to the typical peaks at 284.8 eV (C–C/C=C) and 288.4 eV (N–C=N), Cu–CN exhibits an additional C≡N component at 286.2 eV [51,52]. This C≡N component is consistent with the FTIR band at 2180 cm^{-1}, thereby linking the spectroscopic signatures from FTIR and XPS and further supporting partial C—N bond cleavage within the g–C_3N_4 framework and the introduction of N_v–related defects.

Following the identification of Cu_2O nanocrystalline domains by HRTEM, Cu 2p XPS and Cu LMM AES were employed to determine the surface Cu valence states, while O 1 s XPS was used to examine the evolution of oxygen-containing surface species. In the Cu 2p spectra (Fig. S4b), the Cu $2p_{3/2}$ region of Cu–CN–400 and Cu–CN–450 was deconvoluted into Cu^+ (~932.5 eV) and Cu^{2+} (~934.5 eV) contributions, accompanied by Cu^{2+} satellite peaks [53,54], indicating the coexistence of Cu^+ and Cu^{2+} species. Upon increasing the calcination temperature to 500 °C, the Cu^{2+} signal was markedly weakened, suggesting that Cu^+ was the dominant surface species in Cu–CN–500. Cu LMM AES (Fig. S5b) was conducted to distinguish Cu^+ from Cu^0. Cu–CN–500 displayed the characteristic Cu^+ signal of Cu_2O at approximately 916.0 eV, whereas the metallic Cu^0 signal (~918.6 eV) was

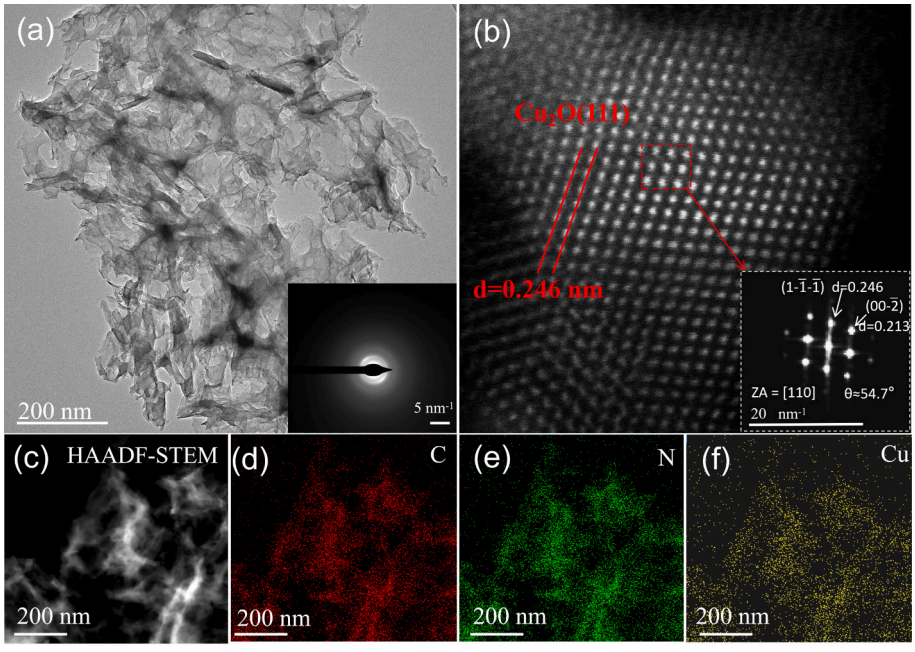

Fig. 2. Morphological and structural characterisation of Cu–CN–500: (a) TEM image with the corresponding SAED pattern shown in the inset; (b) HRTEM image of a selected Cu_2O nanocrystalline domain with the corresponding FFT pattern shown in the inset; (c) HAADF–STEM image and (d–f) the corresponding EDS elemental mappings of C, N, and Cu.

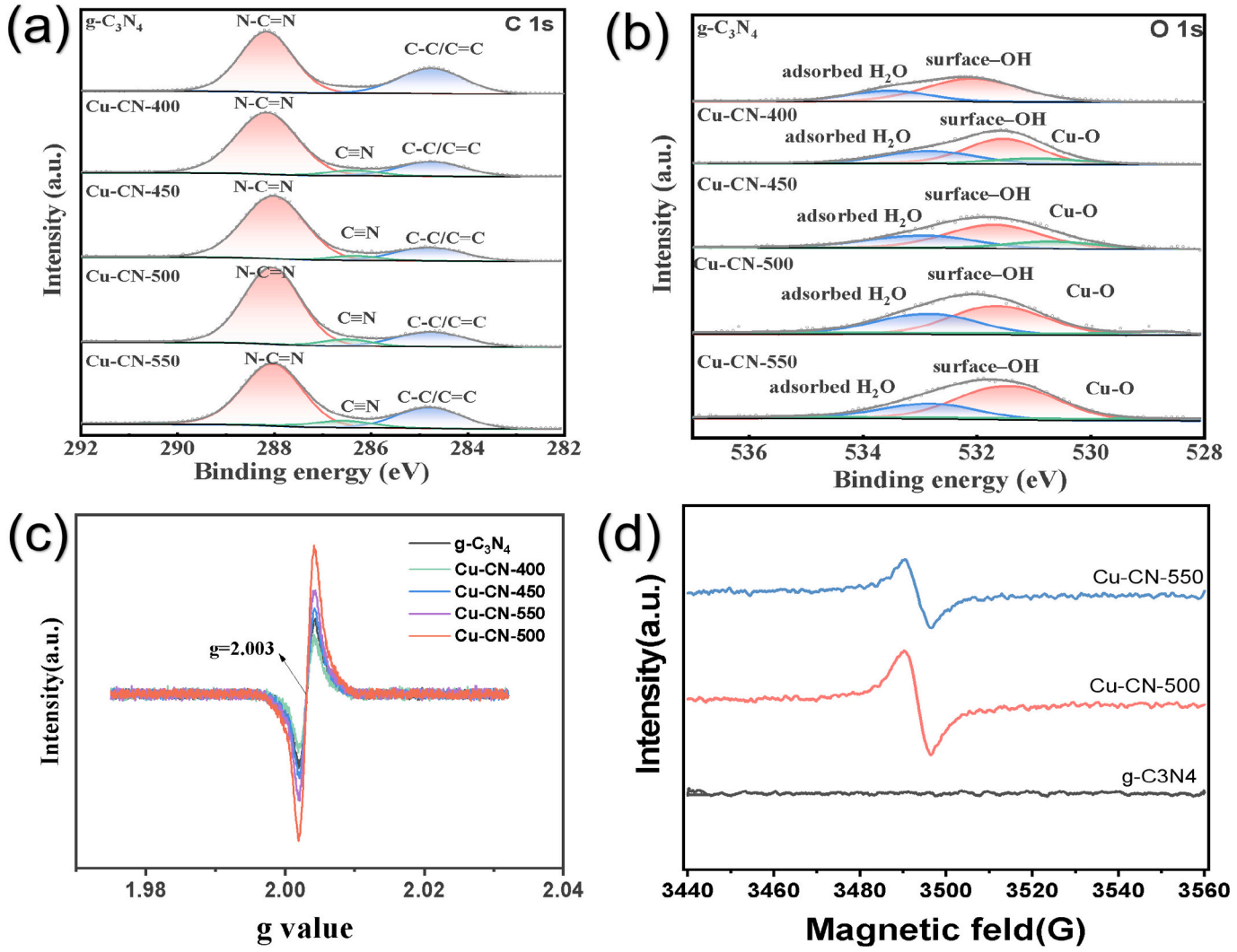

Fig. 3. Surface chemical states and defect-related paramagnetic characteristics of Cu–CN catalysts: high–resolution XPS spectra of (a) C 1 s and (b) O 1 s; (c) solid–state EPR spectra; and (d) solid-state EPR spectra of g-C_3N_4, Cu-CN-500, and Cu-CN-550 recorded under identical conditions.

absent [55,56]. These results indicate that Cu species in fresh Cu–CN predominantly exist as Cu_2O. Therefore, the XPS and Cu LMM AES results, together with HRTEM observations, confirm the formation of highly dispersed low–valence Cu_2O nanoclusters on the defect–evolved CN matrix. Further, the O 1 s spectrum (Fig. 3b) was deconvoluted into Cu—O (528.8 eV), surface –OH (531.6 eV), and adsorbed H_2O (532.8 eV) components [57,58]. Within the Cu–CN series, the surface –OH contribution increased with the evolution of Cu_2O–associated interfacial structures, suggesting the formation of hydroxylated interfacial sites favourable for O_3 adsorption and activation.

Finally, EPR and EIS analyses were employed to connect these structural and chemical features with the electronic properties of Cu–CN. Solid–state EPR measurements further verified the formation of defect structures. As shown in Fig. 3c, all Cu–CN samples exhibited a characteristic signal at g ≈ 2.003, which is commonly attributed to delocalised unpaired electrons in the conjugated π system or defect–associated localised electrons. Compared with pristine CN, Cu–CN showed a markedly stronger EPR signal, indicating that N_v introduction disrupted the local charge balance and promoted accumulation of unpaired electrons around defect sites [59,60]. Under identical measurement conditions, Cu–CN–500 exhibited a stronger EPR signal than Cu–CN–550 suggesting a relatively higher abundance of paramagnetic defect centres in the optimised sample (Fig. 3d). Together with the FTIR and XPS results, the EPR analysis provides complementary evidence for the formation and evolution of N_v-related defect structures (Table S7). The temperature–dependent Raman spectral changes (Fig. S7) further indicate structural evolution of the g–C_3N_4 framework, consistent with the defect evolution revealed by EPR and XPS. The Nyquist plots (Fig. S6) show that Cu–CN–500 exhibits a substantially lower interfacial charge–transfer resistance than Cu–CN–450, indicating facilitated interfacial electron transfer after appropriate defect engineering. This improved electron–transfer capability is expected to promote ozone activation. Combined with the structural characterisation results, the superior catalytic performance of Cu–CN–500 is attributed to the synergistic optimisation of interfacial electron transfer, Cu_2O stabilisation, nitrogen–vacancy construction, and surface hydroxyl enrichment, rather than electron–transfer resistance alone.

3.2. Catalytic performance

3.2.1. Evaluation of Cu–CN for the catalytic ozonation of sodium oxalate

Sodium oxalate ($Na_2C_2O_4$), a refractory pollutant, was selected as a model compound to evaluate the O_3 activation performance of the Cu–CN catalyst. As shown in Fig. S8, oxalate removal solely by physical adsorption was below 5% for all tested materials, indicating a limited adsorption capacity toward oxalate. As shown in Fig. 4a, the O_3–alone system removed only 35% of oxalate within 30 min. The addition of pristine g–C_3N_4 did not produce a discernible improvement in

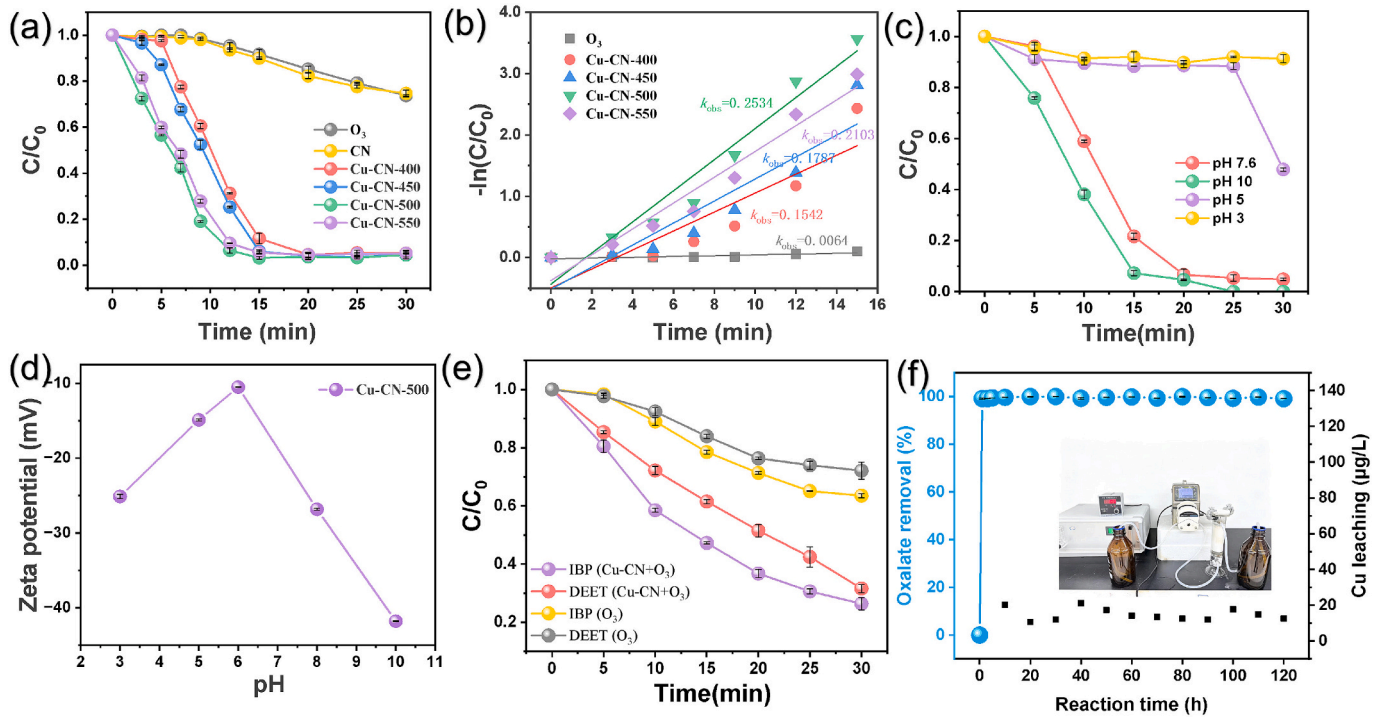

Fig. 4. Catalytic performance, environmental adaptability, and operational stability of the Cu–CN/O_3 system: (a) oxalate degradation over Cu–CN catalysts calcined at different temperatures; (b) corresponding pseudo–first–order kinetic fits; (c) effect of initial pH on the catalytic activity of the Cu–CN–500/O_3 system; and (d) zeta potential of Cu–CN–500 as a function of pH. (e) degradation of IBP and DEET over the O_3-alone and Cu–CN–500/O_3 systems; and (f) long-term continuous-flow catalytic ozonation performance of Cu–CN: oxalate removal efficiency and Cu leaching during 120 h operation. Experimental conditions: [$Na_2C_2O_4$] = 100 mg L^{-1}; [catalyst] = 0.1 g L^{-1}; O_3 feed rate = 0.58 mg min^{-1}; T = 25 °C, unless otherwise specified.

degradation efficiency, suggesting that the CN support limited the intrinsic O_3 activation capability. In contrast, the Cu–CN–500/O_3 system achieved over 99% oxalate removal within 15 min, demonstrating markedly enhanced catalytic ozonation activity. To further benchmark the catalytic performance of Cu–CN–500, representative oxalic acid/oxalate catalytic ozonation systems reported in the literature were compared (Table S4). Although differences in the oxalate source, catalyst dosage, O_3 dosage, pH, and reaction time should be taken into account, Cu–CN–500 achieved over 99% oxalate removal within only 15 min, corresponding to a high apparent rate constant of 0.253 min^{-1} at a low catalyst dosage of 0.10 g L^{-1} and an O_3 dosage of 0.58 mg min^{-1}. These results demonstrate that Cu–CN–500 exhibited competitive catalytic activity and mineralization performance under mild conditions [25,26,61–63].

To further evaluate the mineralization capability of the catalytic ozonation system, total organic carbon (TOC) removal was determined. As shown in Fig. S9, the TOC removal efficiency of the Cu–CN/O_3 system gradually increased to approximately 84% after 200 min. Although oxalate was almost completely removed within 15 min, the substantially slower TOC removal suggests the presence of residual organic carbon or possible analytical and carbon-mass-balance effects; however, the nature of this residual carbon was not fully resolved. Compared with O_3 alone (≈35%) and pristine g–C_3N_4/O_3 (≈42%), the Cu–CN/O_3 system exhibited a higher TOC removal efficiency (≈84%), demonstrating its enhanced overall mineralization performance under the tested conditions.

3.2.2. *Optimisation of Cu–CN catalyst preparation parameters*

The calcination temperature and Cu dosage strongly influence the structure and catalytic performance of Cu–CN. To determine the optimal thermal treatment condition, Cu–CN–T samples were prepared at different calcination temperatures at a fixed Cu dosage of 0.15 × 10^{-3} mol. As shown in Fig. 4a, the time required to achieve near–complete oxalate degradation decreased markedly as the calcination temperature increased from 400 to 500 °C, suggesting that moderate thermal treatment favours the formation of effective Cu–CN interfacial active regions. However, a further increase to 550 °C led to a reduction in catalytic activity, indicating that a higher calcination temperature does not necessarily generate more catalytically effective sites. Specifically, excessive thermal treatment generates a less favourable structural and electronic environment at the Cu–CN interface, thereby reducing the efficiency of interfacial electron transfer and O_3 activation. Pseudo–first–order kinetic fitting (Fig. 4b, $R^2 > 0.98$) yielded apparent rate constants (k_{obs}) of 0.1542, 0.1787, 0.2534, and 0.2103 min^{-1} for Cu–CN–400, Cu–CN–450, Cu–CN–500, and Cu–CN–550, respectively. Among these, Cu–CN–500 exhibited the highest k_{obs}, approximately 39–fold higher than that of the O_3–alone system, indicating that calcination at 500 °C provides a more favourable structural balance for efficient catalytic ozonation. XRF analysis revealed comparable Cu loadings of 11.3–12.5 wt% across the Cu–CN–T series (Table S5), indicating that the activity differences primarily arose from calcination–induced changes in interfacial structure and electronic properties rather than variations in Cu loading. Under identical O_3-feed conditions, Cu–CN–500 exhibited the highest ozone utilization efficiency among the catalyst series (Fig. S10), consistent with its highest apparent reaction rate, indicating more efficient ozone activation rather than differences in Cu loading.

Similarly, to determine the optimal Cu dosage, Cu–CN–x samples were prepared by varying the Cu dosage from 0.05 to 0.20 × 10^{-3} mol at 500 °C. The influence of Cu precursor dosage on catalytic performance is shown in Fig. S11. At a Cu dosage of 0.15 × 10^{-3} mol, Cu–CN–0.15 achieved the maximum k_{obs}, which was 9.0% higher than that of Cu–CN–0.05. However, when the Cu dosage was further increased to 0.20 × 10^{-3} mol, k_{obs} decreased by 38.0% relative to the optimal sample. These results indicate that an appropriate dosage of Cu promotes the formation of effective Cu–CN interfacial active regions and enhances O_3

activation, whereas excessive Cu may lead to aggregation, shielding of active sites, or disruption of the interfacial structure, thereby impairing catalytic performance.

3.2.3. Environmental adaptability and operational stability of the Cu–CN/O_3 system

The influence of initial pH on the catalytic performance of the Cu–CN–500/O_3 system was investigated (Fig. 4c). Oxalate degradation increased markedly with increasing initial pH. Although the reaction was inhibited under acidic conditions, high degradation efficiencies were achieved at the unadjusted initial pH (~7.6) and under alkaline conditions. Consistent with the zeta–potential results (Fig. 4d), Cu–CN–500 was negatively charged across the tested pH range, indicating electrostatic repulsion between the catalyst and anionic oxalate species, consistent with the weak adsorption observed.

Therefore, the enhanced degradation under alkaline conditions cannot be attributed to adsorption effects. Instead, OH^- initiates the radical-chain decomposition of ozone, while the Cu–CN catalyst further promotes catalytic ozone activation, jointly enhancing ROS generation [64]. Nevertheless, excessively alkaline conditions may accelerate ozone decay before ozone can effectively participate in catalytic oxidation, thereby decreasing the effective utilization of ozone for pollutant degradation [2,64]. Consequently, the catalytic performance is governed by the balance between ROS generation and ozone utilization. To further verify that this interpretation was not influenced by reaction-induced pH variation, the solution pH was continuously monitored throughout the reaction (Fig. S12). The pH increased only slightly from approximately 7.6 to 8.1 over 120 min, corresponding to a variation of approximately 0.5 pH units. Such a minor change indicates that the bulk-solution pH remained essentially stable during the reaction, confirming that the observed catalytic behaviour was not significantly affected by reaction-induced pH variation.

To evaluate the applicability of the Cu–CN/O_3 system under more realistic water conditions, the effects of typical inorganic anions (Cl^-, SO_4^{2-}, and HCO_3^-) on catalytic performance were examined (Fig. S13a). High concentrations of Cl^- and SO_4^{2-} caused only minor kinetic inhibition of oxalate degradation, whereas the addition of HCO_3^- reduced the degradation rate during the initial reaction stage. Nevertheless, the system still achieved over 90% oxalate removal after 25 min. These results demonstrate that the Cu–CN/O_3 system maintains high catalytic efficiency in the presence of coexisting anions, indicating good tolerance to water–matrix interference and potential practical applicability. The applicability of the Cu–CN/O_3 system was further assessed using ibuprofen (IBP) and N,N–diethyl–m–toluamide (DEET) as additional refractory micropollutants and surface water, tap water, and secondary effluent as realistic water matrices (Fig. 4e). Cu–CN/O_3 achieved approximately 74% IBP removal and 69% DEET removal within 30 min, markedly exceeding the corresponding O_3–alone removals of approximately 37% and 28%, respectively. Cu–CN also consistently enhanced oxalate degradation in all tested water matrices, although partial inhibition was observed because of matrix competition. These results demonstrate that the O_3–activation capability of Cu–CN extends beyond oxalate and remains effective in complex aqueous environments (Fig. S13b).

To further evaluate the long–term operational stability of the Cu–CN/O_3 system under conditions more relevant to practical application, a continuous–flow catalytic ozonation experiment was conducted. As shown in Fig. 4f, after a short start–up period, the oxalate removal efficiency stabilised at approximately 100% and remained within this range throughout 120 h of continuous operation. Meanwhile, the inlet and outlet gas–phase ozone concentrations were monitored during continuous operation, giving an ozone utilization efficiency of 80.9%. Moreover, the dissolved Cu concentration was consistently maintained at only 10–20 μg L^{-1}, indicating negligible Cu leaching during continuous operation. These results demonstrate the robust operational stability of the Cu–CN/O_3 system under continuous ozonation conditions. Consistent with the continuous–flow results, Cu–CN also retained over 90% oxalate removal after five consecutive batch cycles (Fig. S14), further confirming its good catalyst reusability.

To examine whether prolonged continuous ozonation altered the catalyst structure, the fresh and recovered Cu–CN catalysts were characterized by XRD, Cu LMM Auger spectroscopy, TEM, HAADF imaging, and Cu elemental mapping (Fig. S5). The nearly identical XRD patterns (Fig. S5a) indicate that no detectable bulk phase transformation occurred after prolonged operation. Meanwhile, the Cu LMM spectra (Fig. S5b) remained dominated by the characteristic Cu(I) feature at approximately 916 eV, confirming that Cu(I) was still the predominant Cu species. TEM, HAADF imaging, and elemental mapping (Fig. S5c) further revealed that the nanosheet morphology and homogeneous Cu distribution were well preserved without noticeable aggregation or migration. Although weak Cu(II) components were observed in the Cu 2p spectra (Fig. S15), they only indicate limited surface oxidation and are consistent with the Cu LMM results. These post–reaction characterisation results indicate that Cu(I) remained the predominant Cu species, despite limited surface oxidation, and that the highly dispersed Cu–containing interfacial structure was largely preserved after prolonged catalytic ozonation.

3.3. Catalytically active sites and mechanisms

3.3.1. Identification of catalytically active sites

Catalytic performance evaluation revealed that Cu–CN–500 exhibited the highest activity among the temperature–varied samples, suggesting that calcination at 500 °C favours the formation of catalytically effective interfacial structures. Combined with the findings of HRTEM, XPS, and Cu LMM AES analyses, the enhanced catalytic performance of Cu–CN can be attributed to the formation of highly dispersed low–valence Cu_2O nanoclusters on the g–C_3N_4 matrix. However, the control experiment in Fig. S16 shows that pristine Cu_2O exhibited only limited activity toward oxalate degradation, suggesting that Cu_2O does not function as an efficient isolated active phase. These results suggest that the catalytic role of Cu_2O is substantially enhanced when it is highly dispersed and electronically coupled with the defective g–C_3N_4 substrate, thereby promoting the formation of effective interfacial sites for O_3 adsorption and activation. Therefore, Cu incorporation is essential for improving the catalytic performance of Cu–CN, but the enhanced activity mainly originates from the Cu_2O/defective g–C_3N_4 interfacial structure rather than from isolated Cu_2O species.

To further probe the potential active sites responsible for O_3 activation, the structure–activity relationship between the apparent rate constant (k_{obs}) and surface oxygen–containing species was established (Fig. 5a). A strong positive correlation was observed between k_{obs} and the surface –OH content, suggesting that surface hydroxylated species contribute to the enhanced catalytic activity and may serve as important interfacial sites for O_3 activation. To validate the role of surface –OH sites, phosphate (PO_4^{3-}) was employed as a competitive site–blocking probe. As a strong Lewis base, PO_4^{3-} can preferentially interact with surface Lewis–acidic metal sites and hydroxylated interfacial sites, thereby blocking –OH–dependent interfacial reaction pathways. Meanwhile, its relatively low rate constant for reaction with •OH ($k < 1 \times 10^7$ M^{-1} s^{-1}) compared with typical •OH scavengers minimizes interference from the direct quenching of bulk–phase •OH [38]. As shown in Fig. S17, PO_4^{3-} inhibited oxalate degradation in a pronounced, concentration–dependent manner, with significant suppression at 10 mM. This behaviour validates that surface hydrated hydroxyl groups serve as catalytically relevant interfacial sites in the Cu–CN/O_3 reaction, rather than merely as spectator species. Moreover, the surface –OH content increased with calcination temperature and was consistent with the formation of Cu_2O–related interfaces (Fig. 5b), implying that Cu_2O containing interfacial structures favour the stabilisation and enrichment of surface hydroxyl species.

Further, DFT calculations (Fig. 5b) show that the OH–Cu_2O–CN

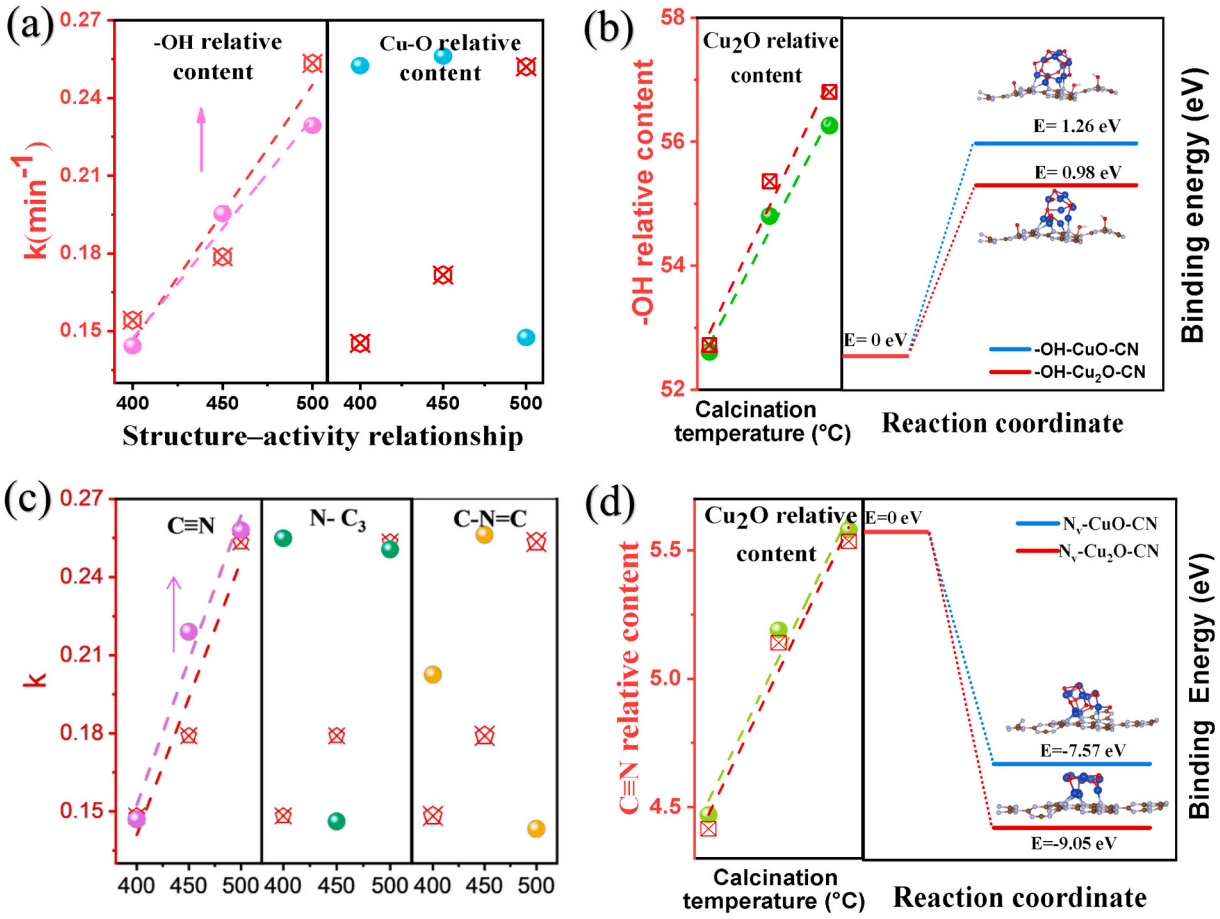

Fig. 5. Structure–activity relationships and theoretical analysis of active interfacial sites in the Cu–CN/O_3 system: (a) correlations of k_{obs} with surface –OH and Cu—O species; (b) temperature-dependent evolution of surface –OH and Cu_2O, together with calculated energy profiles for –OH stabilisation at CuO–CN and Cu_2O–CN interfaces; (c) correlations of k_{obs} with surface N species; and (d) coupled evolution of C≡N and Cu_2O, together with the calculated binding energies of the N_v–CuO–CN and N_v–Cu_2O–CN configurations.

configuration exhibits a lower calculated energy for –OH stabilisation than the OH–CuO–CN configuration (0.98 and 1.26 eV, respectively). This result suggests that the Cu^+–rich Cu_2O–related interface provides a more favourable interfacial environment for stabilizing surface –OH species. In addition, NH_3–TPD profiles (Fig. S18a) show that Cu–CN–500 exhibits intensified NH_3 desorption extending into the high–temperature region, with the total acidity increasing from 1.96×10^{-3} mol g^{-1} for pristine g–C_3N_4 to 2.86×10^{-3} mol g^{-1} after Cu_2O incorporation. These results indicate that coupling Cu_2O with defective g–C_3N_4 modifies the interfacial acid environment, thereby facilitating water adsorption and polarisation. To further probe the interfacial environment relevant to hydroxyl formation, H_2O–TPD measurements were performed (Fig. S18b). Compared with pristine g–C_3N_4, Cu–CN exhibits significantly stronger H_2O desorption in the 150–350 °C region, indicating enhanced water adsorption at the Cu_2O/g–C_3N_4 interface. These results suggest that the interfacial structure provides favourable conditions for hydroxyl formation, which is further verified by the subsequent in situ DRIFTS analysis. Collectively, the correlation analysis, phosphate inhibition experiments, DFT calculations, and TPD characterisation consistently indicate that hydrated hydroxyl species are preferentially stabilised at the Cu_2O/defective g–C_3N_4 interface and are closely associated with the enhanced ozone activation performance.

The incomplete inhibition observed in the phosphate–blocking experiment further suggests that, in addition to phosphate–sensitive surface hydroxyl sites, other interfacial sites or synergistic pathways may also contribute to oxalate degradation in the Cu–CN/O_3 system. Accordingly, the structure–activity relationship between the apparent rate constant k_{obs} and nitrogen–containing species was established (Fig. 5c). The results showed that k_{obs} exhibited a strong positive correlation with the C≡N content, whereas the content of N–$(C)_3$ framework–bridging nitrogen was negatively correlated with k_{obs}. These correlations were mainly established within the catalytically favourable calcination temperature range of 400–500 °C, while the over–calcined Cu–CN–550 sample deviated from this trend due to its less favourable interfacial electronic environment.

Given that C≡N species generally originate from partial C—N bond cleavage within the g–C_3N_4 framework and serve as structural indicators of N_v formation, the positive correlation between C≡N content and k_{obs} indicates that C ≡ N–associated, N_v–related defect structures are closely linked to the enhanced catalytic activity of the Cu–CN/O_3 system. The relative content of C≡N species exhibited a positive linear correlation with the relative content of Cu_2O (Fig. 5d), suggesting the coupled formation/evolution of N_v–related defect structures and low–valence Cu_2O species during thermal treatment. This correlation indicates that N_v–related defects are closely associated with the formation and stabilisation of Cu_2O–containing interfacial structures. DFT calculations (Fig. 5d) further reveal that the N_v–Cu_2O–CN configuration possesses a more negative binding energy than the N_v–CuO–CN configuration, with values of −9.05 and − 7.57 eV, respectively. The stronger binding interaction indicates that Cu_2O is more strongly stabilised than CuO on the N_v–defective CN substrate, supporting the preferential anchoring of Cu^+–rich Cu_2O species at N_v–related defect sites. This provides theoretical evidence for the formation and stabilisation of low–valence Cu species at the CN–based reaction interface. Therefore, N_v sites may

contribute to the catalytic activity by serving as defect–associated interfacial sites and, more importantly, acting as anchoring/stabilisation centres for Cu_2O nanoclusters on the g–C_3N_4 substrate, thereby constructing a robust N_v–Cu_2O coupled interface with enhanced interfacial electronic coupling. It should be noted that the N_v discussed here refers to N_v–related defect structures rather than a single isolated vacancy. Since vacancy activity depends on local defect arrangement, the enhanced performance of Cu–CN is attributed to favourable N_v–related interfacial configurations.

Overall, the catalytically relevant interfacial features in the Cu–CN/O_3 system comprise dynamically evolved hydroxylated surface species together with N_v–anchored low–valence Cu_2O interfacial sites. Specifically, the in situ DRIFTS results (Section 3.3.2) suggest that hydroxyl–related surface species dynamically participate in interfacial O_3 adsorption and activation rather than merely existing as spectator species. These hydroxylated interfacial sites are therefore considered to play a key role in facilitating ozone activation. N_v acts as a defect–anchoring centre, stabilizing low–valence Cu_2O nanoclusters and contributing to the construction of a stable defective Cu_2O–CN interfacial structure. As the dominant Cu active phase, Cu_2O not only promotes surface –OH enrichment but also forms a stable coupled interface with N_v. Collectively, these findings support the interpretation that the enhanced catalytic activity of Cu–CN is associated with the cooperative contributions of dynamically evolving hydroxyl–related surface species, N_v–related defect structures, and low–valence Cu_2O interfacial sites. These features favour interfacial electronic coupling, O_3 adsorption, and subsequent activation.

3.3.2. *In situ DRIFTS evidence for the dynamic evolution of hydroxylated surface species during ozone activation*

To provide direct experimental evidence for the evolution of surface species during ozone activation, in situ DRIFTS measurements were performed on pristine g–C_3N_4 and Cu–CN under an identical dry N_2/O_3 atmosphere. This experiment was designed to monitor the dynamic evolution of surface species during ozone exposure and to clarify whether the Cu_2O/defective–g–C_3N_4 interface alters the surface reaction process beyond the static structural information obtained from XPS and FTIR. Particular attention was paid to the broad 3300–3700 cm^{-1} region, corresponding to the overlapping stretching vibrations of surface hydroxyl species in the carbon nitride framework.

As shown in Fig. S19, pristine g–C_3N_4 exhibits only slight spectral evolution throughout ozone exposure, indicating that the surface environment remains nearly unchanged under the experimental conditions. In contrast, Cu–CN displays a pronounced time–dependent enhancement and broadening of the O—H stretching envelope with increasing ozone exposure time. Since both catalysts were measured under identical dry N_2/O_3 conditions, the much stronger spectral evolution observed for Cu–CN suggests that the defect-engineered Cu_2O/g–C_3N_4 interface facilitates the redistribution and transformation of pre-existing hydroxylated surface species during ozone activation, rather than simply containing a higher abundance of these species. It should be noted that the narrow spectral features appearing in the 1500–1700 cm^{-1} region were not used as the primary basis for mechanistic interpretation. This spectral region overlaps with the C=N/C–N vibrations of the g–C_3N_4 framework and may also be affected by gas–phase or background subtraction under flowing ozone. Therefore, the mechanistic discussion mainly relies on the evolution of the broad O—H stretching region, which provides more reliable evidence for the dynamic surface process.

The in situ DRIFTS results therefore provide direct experimental evidence that hydroxylated surface species are dynamically involved in interfacial ozone activation over Cu–CN. These time–resolved spectral changes reflect the redistribution and transformation of hydroxyl–related surface species during O_3 exposure, rather than merely confirming the static presence of surface hydroxyl groups. Although other interfacial processes associated with Cu_2O species and nitrogen vacancies may contribute to ozone activation, the pronounced evolution of hydroxyl-related signals indicates that surface hydroxyl species serve as catalytically relevant interfacial species during this process. When considered together with the O 1 s XPS results indicating an increased contribution from hydroxyl-related oxygen species, the EIS results indicating accelerated interfacial electron transfer, the EPR analysis identifying enhanced ROS generation, and the DFT calculations demonstrating more favourable O_3 adsorption and –OH stabilisation on the defect–engineered interface, the results consistently support a cooperative interfacial activation mechanism. In this mechanism, nitrogen vacancies regulate interfacial electronic redistribution and stabilize Cu_2O nanoclusters, while the dynamically evolved hydroxylated surface species facilitate interfacial O_3 adsorption and activation, thereby jointly promoting ROS generation and efficient oxalate degradation.

3.3.3. *ROS generation mechanism*

To identify the major ROS involved in oxalate degradation, systematic radical–quenching experiments were conducted. Tert–butanol (TBA, •OH probe, $k_{\bullet OH} = 5.2 \times 10^{10}\ M^{-1}\ s^{-1}$), *p*–benzoquinone (BQ, $O_2^{\bullet-}$ scavenger), and catalase (CAT, H_2O_2 probe, $k_{H_2O_2} = 2.0 \times 10^{9}\ M^{-1}\ s^{-1}$) [65] were used as scavengers/probes. As shown in Fig. 6a, compared with the scavenger–free control, the addition of TBA, BQ, and CAT inhibited oxalate degradation to different extents. The relative roles of the ROS were inferred from the apparent inhibition efficiencies rather than assigned as exact quantitative contributions, because the scavengers differ in selectivity and may also perturb the interconnected ROS reaction network. The pronounced inhibition caused by BQ, together with the distinct DMPO–$O_2^{\bullet-}$ signal, suggests that $O_2^{\bullet-}$ plays an important role in O_3 activation. Meanwhile, the inhibition caused by TBA, along with the DMPO–•OH signal, provides direct evidence for the involvement of •OH in oxalate oxidation. The comparatively weaker effect of CAT suggests that H_2O_2 mainly participates as an intermediate in ROS conversion rather than acting as the dominant oxidant.

EPR spin–trapping measurements further confirmed the in–situ generation of ROS. As shown in Fig. 6b, characteristic DMPO–•OH adduct signals are present in all Cu–CN/O_3 systems, exhibiting the typical 1:2:2:1 quartet pattern with hyperfine coupling constants of $\alpha N = \alpha H\beta = 14.9$ G. Conversely, much weaker signals were observed in the O_3–alone and g–C_3N_4/O_3 systems, indicating that Cu–CN substantially promoted •OH generation. As shown in Fig. 6c, the DMPO–•OH signal intensity increased with the catalytic activity of Cu–CN–400, Cu–CN–450, and Cu–CN–500, suggesting that •OH generation is closely associated with oxalate degradation efficiency and represents an important factor governing catalytic performance. In addition, Fig. S20 reveals distinct DMPO–$O_2^{\bullet-}$ adduct signals in the Cu–CN/O_3 system and weak signals in the O_3–alone and g–C_3N_4/O_3 systems, indicating that Cu–CN facilitated single–electron reduction of O_3 to generate $O_2^{\bullet-}$ intermediates. The good agreement between the EPR measurements and radical–quenching experiments provides complementary evidence for the participation of both •OH and $O_2^{\bullet-}$ during catalytic ozonation.

Overall, the radical–quenching and EPR results consistently indicate that •OH is the predominant reactive species responsible for oxalate degradation in the Cu–CN/O_3 system, whereas $O_2^{\bullet-}$ primarily acts as a key intermediate during ozone activation. Based on the inhibition experiments, the apparent contributions of •OH–mediated oxidation, $O_2^{\bullet-}$–related processes, and residual/direct O_3 oxidation were approximately 64%, 16%, and 20%, respectively (Fig. 6d). These values should be regarded as apparent kinetic contributions rather than independent oxidation pathways, since $O_2^{\bullet-}$ and •OH are generated sequentially through the ozone decomposition cascade and are intrinsically coupled. This interpretation is consistent with previous studies on catalytic ozonation [7]. Overall, the combined experimental evidence supports that ozone activation over the Cu–CN catalyst proceeds predominantly via a radical–mediated pathway, while minor contributions from surface–bound reactive species or interfacial non–radical electron–transfer processes cannot be completely excluded.

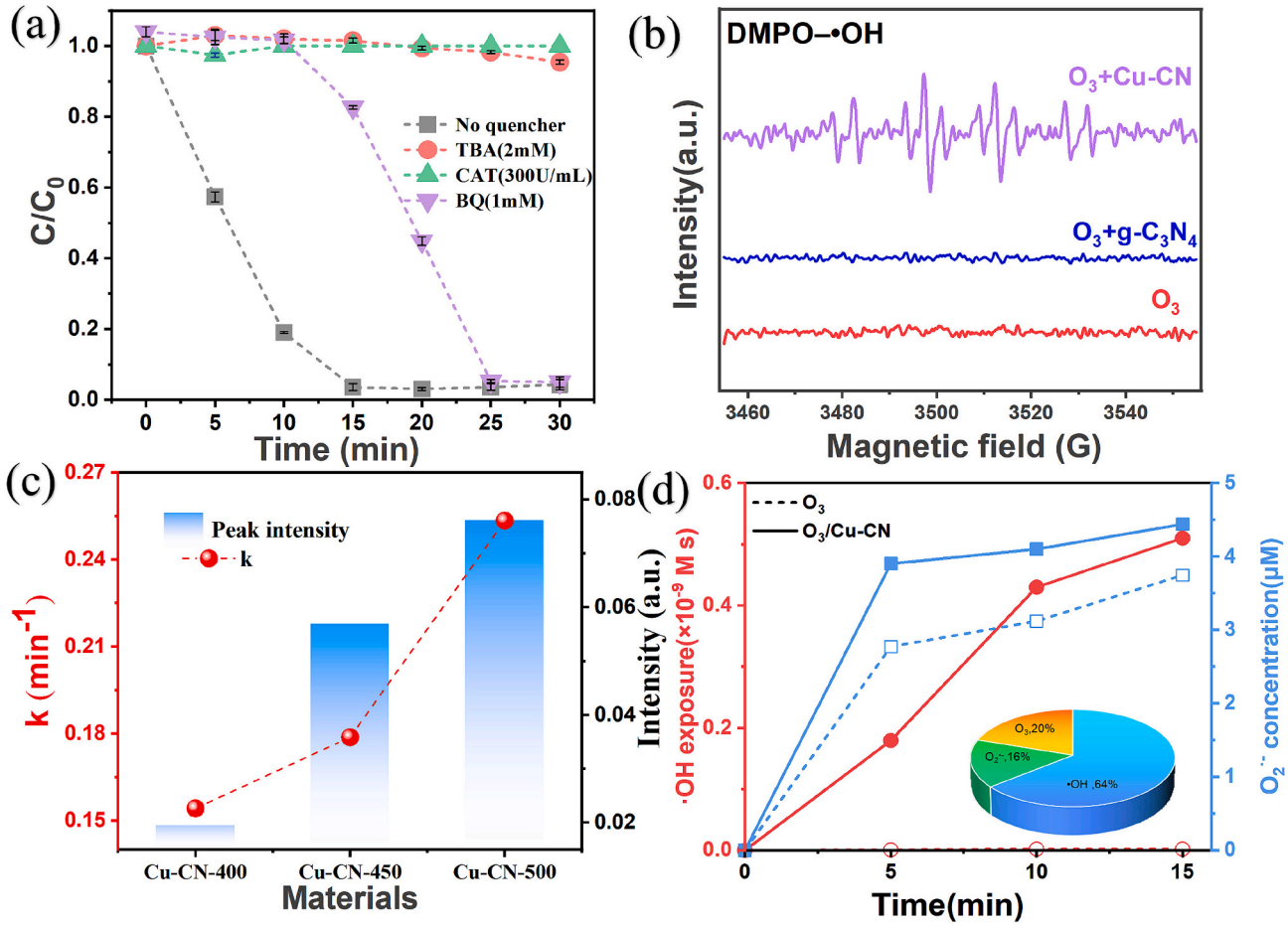

Fig. 6. Identification and apparent kinetic assessment of reactive oxygen species in the Cu–CN/O_3 system: (a) effects of different scavengers on oxalate degradation; (b) EPR spin-trapping spectra of DMPO–•OH adducts; (c) correlation between kobs and the DMPO–•OH signal intensity; and (d) estimated relative contributions of reactive oxygen species and direct O_3 oxidation. Unless otherwise specified, the reaction conditions were the same as those described in Fig. 4; [TBA] = 2 mM, [BQ] = 1 mM, and [CAT] = 300 U mL^{-1}.

3.3.4. *DFT calculations and synergistic mechanisms*

To clarify the initial adsorption and electronic interaction of O_3 at the Cu–CN interface, DFT calculations were conducted to evaluate adsorption energetics, interfacial charge transfer, and adsorption–induced

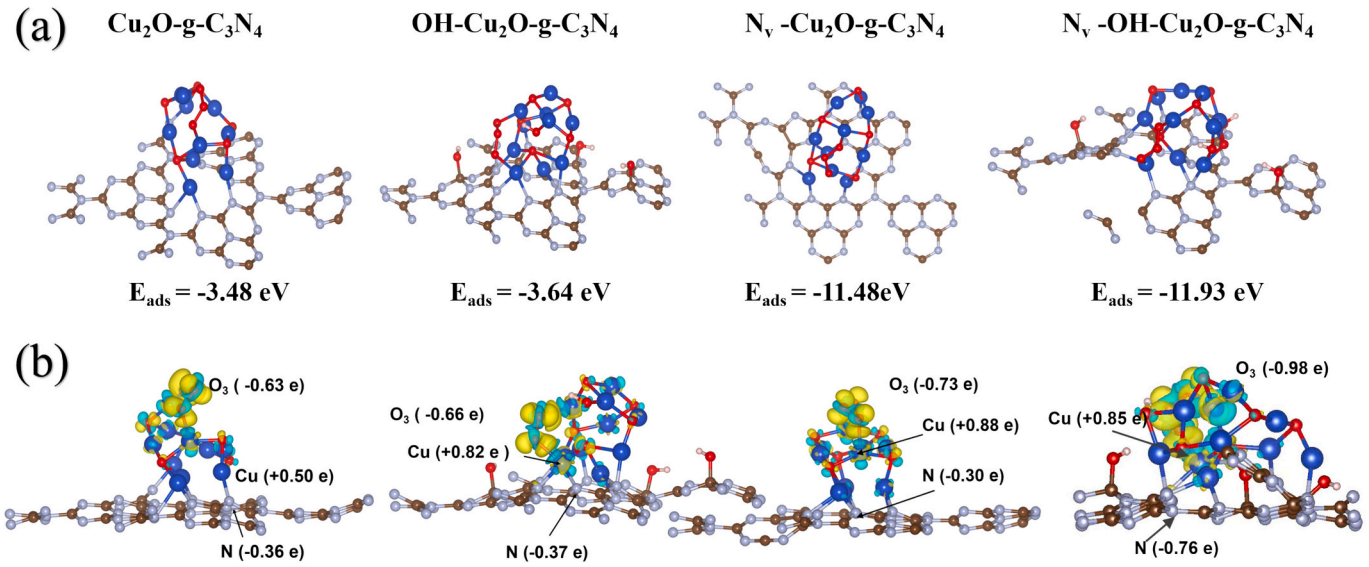

Fig. 7. DFT analysis of O_3 adsorption, activation, and interfacial charge transfer on different Cu_2O/g–C_3N_4 interfaces: (a) optimised O_3 adsorption configurations and corresponding adsorption energies and overall energy changes on Cu_2O–g–C_3N_4, OH–Cu_2O–g–C_3N_4, N_v–Cu_2O–g–C_3N_4, and N_v–OH–Cu_2O–g–C_3N_4; and (b) corresponding charge-density-difference maps and Bader charge-transfer values.

O—O bond perturbation. Based on the active–site analysis described in section 3.3.1, Cu_2O–g–C_3N_4, OH–Cu_2O–g–C_3N_4, N_v–Cu_2O–g–C_3N_4, and N_v–OH–Cu_2O–g–C_3N_4 models were constructed, with the N_v–OH–Cu_2O–g–C_3N_4 model representing the key active interfacial structure of Cu–CN, to evaluate the effects of Cu_2O, surface –OH, and N_v on O_3 activation. All adsorption configurations were fully optimised without geometric constraints on the O_3 molecule, thereby allowing spontaneous structural evolution, including O—O bond elongation, molecular distortion, and possible dissociation, during geometry optimisation.

As shown in Fig. 7a, the adsorption energy of O_3 on the Cu_2O–g–C_3N_4 surface was −3.48 eV, indicating that the supported Cu_2O interface can effectively adsorb O_3. After introducing surface –OH, the adsorption energy for the OH–Cu_2O–g–C_3N_4 configuration became more negative (−3.64 eV), suggesting that surface –OH further stabilizes molecular O_3 adsorption at the Cu_2O interface. In both configurations, O_3 remained molecularly adsorbed after structural optimisation. It should be noted that the significantly higher negative adsorption energies obtained for the N_v–containing models should not be interpreted as conventional molecular O_3 adsorption. During unconstrained geometry optimisation, O_3 underwent pronounced structural distortion accompanied by O—O bond elongation at the N_v–Cu_2O interfacial sites, indicating strongly activated chemisorption and an incipient partial–dissociation process. Accordingly, the calculated overall energy changes of −11.48 and −11.93 eV for the N_v–Cu_2O–g–C_3N_4 and N_v–Cu_2O–OH–g–C_3N_4 models, respectively, which were associated with O_3 dissociative chemisorption and subsequent surface reconstruction rather than simple molecular adsorption. These highly negative values therefore reflect the strong thermodynamic driving force for electron–transfer–assisted O_3 activation at the defect–coupled interfaces [15].

To elucidate the electron–transfer characteristics during O_3 activation, interfacial charge redistribution was further investigated using charge density difference analysis combined with Bader charge analysis. As shown in Fig. 7b, O_3 gained approximately 0.63, 0.66, 0.73, and 0.98 e^- on the Cu_2O–g–C_3N_4, OH–Cu_2O–g–C_3N_4, N_v–Cu_2O–g–C_3N_4, and N_v–OH–Cu_2O–g–C_3N_4 models, respectively. The progressively increased electron gain indicates that both surface –OH and N_v enhance interfacial electron transfer to O_3, with the N_v–OH–Cu_2O–g–C_3N_4 interface exhibiting the strongest electron–donating capability. This substantial charge transfer also explains the pronounced O_3 structural distortion observed after geometry optimisation. In particular, the increase in electron gain from 0.73 e^- on N_v–Cu_2O–g–C_3N_4 to 0.98 e^- on N_v–OH–Cu_2O–g–C_3N_4 suggests a cooperative effect between N_v and surface –OH in promoting interfacial charge injection. The charge density difference maps show pronounced electron accumulation around O_3, accompanied by electron depletion at the Cu_2O–g–C_3N_4 interface, suggesting that electrons are primarily transferred from the Cu_2O–defective g–C_3N_4 interface to adsorbed O_3. Given the strong electrophilicity of O_3, interfacial electron injection is expected to weaken the O—O bonds, thereby facilitating O_3 activation and the formation of reduced oxygen intermediates. In conjunction with the experimental radical–identification results, these intermediates may include $O_2^{\bullet-}$ and/or $O_3^{\bullet-}$, which can subsequently participate in •OH generation.

Based on the experimental results described above and the DFT calculations, a defect–regulated synergistic catalytic mechanism involving two cooperative interfacial contributions—surface hydroxyl enrichment and N_v–mediated Cu_2O anchoring/electronic coupling—is proposed for the Cu–CN/O_3 system (Fig. 8). For the surface–hydroxyl–mediated pathway, Cu_2O–associated interfacial Cu sites facilitate water adsorption and polarisation, favouring the formation of Cu–OH species and surface hydrated hydroxyl groups. The enriched surface –OH groups are therefore considered to provide favourable local environments for O_3 adsorption and interfacial activation, thereby facilitating the subsequent formation of reactive oxygen intermediates. For the defect–mediated interfacial pathway, N_v acts as a defect–anchoring/stabilisation centre for highly dispersed, low–valence Cu_2O nanoclusters, thereby constructing a robust N_v–Cu_2O coupled interface and strengthening interfacial electronic coupling with the CN matrix. This coupled interface further facilitates electron injection into adsorbed O_3, weakening its O—O bonds and promoting the formation of reduced oxygen intermediates such as $O_2^{\bullet-}$/$O_3^{\bullet-}$. These intermediates may subsequently contribute to •OH formation through further interfacial reactions. Finally, •OH and related ROS drive the oxidative degradation of oxalate. Collectively, the cooperative N_v–Cu_2O–OH interface enables efficient O_3 activation by integrating surface hydroxyl–mediated O_3 adsorption/activation, N_v–guided Cu_2O interfacial stabilisation and electronic coupling, and sustained ROS generation, thereby accounting for the high catalytic ozonation performance of the Cu–CN/O_3 system.

4. Conclusions

In this study, a Cu–CN composite catalyst was fabricated through N_v–mediated anchoring of highly dispersed Cu_2O nanoclusters via a supramolecular preassembly–thermal polycondensation strategy. The resulting defect–engineered Cu_2O/defective g–C_3N_4 interface enhanced oxalate degradation during HCO. In addition to enhancing the HCO performance, this study elucidated a cooperative N_v–Cu_2O–OH interfacial structure that governs efficient O_3 activation. Structural

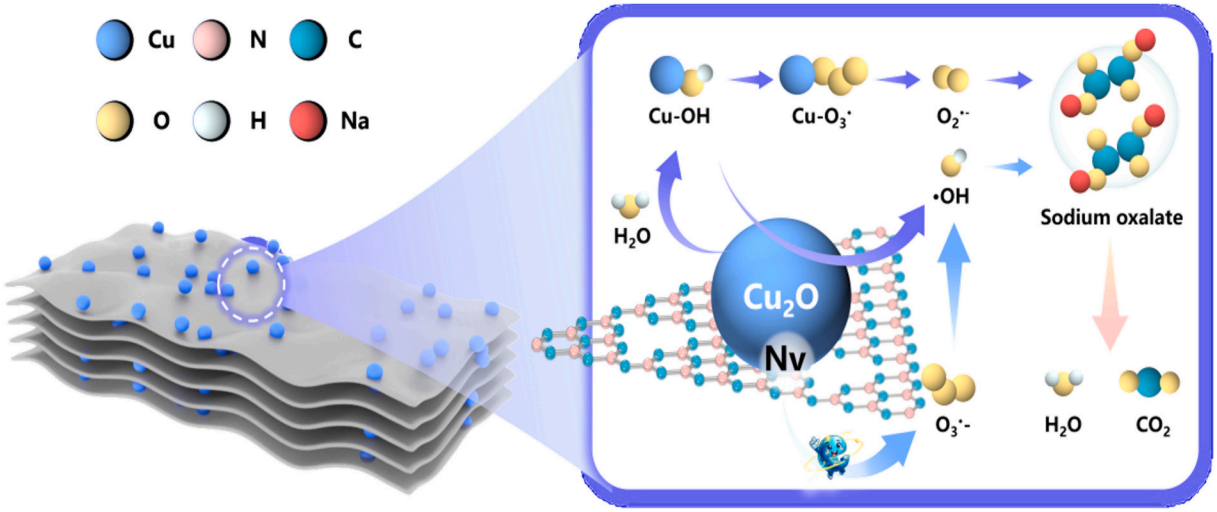

Fig. 8. Proposed mechanism of O_3 activation and oxalate degradation over the cooperative N_v–Cu_2O–OH interface in the Cu–CN/O_3 system.

characterisation, structure–activity correlations, and DFT calculations collectively revealed that the catalytic performance of Cu–CN originates from the coordinated roles of N_v–related defects, low–valence Cu_2O nanoclusters, and surface –OH species. Specifically, surface –OH enrichment provides hydroxylated interfacial sites that participate cooperatively in O_3 adsorption and activation, and N_v–related defects act as anchoring/stabilisation and electronic–regulation centres for low–valence Cu_2O nanoclusters. These defects then guide the construction of a robust N_v–Cu_2O coupled interface and strengthen interfacial electronic coupling between Cu_2O and the g–C_3N_4 matrix. As the dominant interfacial metal active phase, Cu_2O provides Cu–associated sites favourable for water adsorption/polarisation and surface hydroxyl stabilisation. The resulting N_v–Cu_2O–OH interface facilitates electron transfer to adsorbed O_3 and sustains ROS generation involving $O_2^{\bullet-}/O_3^{\bullet-}$ and •OH, thereby enabling efficient oxalate degradation. The Cu–CN–500/O_3 system also enhanced the removal of IBP and DEET and retained appreciable activity in surface water, tap water, and secondary effluent, demonstrating pollutant versatility and water–matrix tolerance under laboratory conditions. In addition, Cu–CN retained good catalytic activity during repeated use and prolonged recirculating operation, with limited Cu leaching, supporting its operational stability under the tested laboratory conditions. Overall, this study clarifies the mechanistic N_v–Cu_2O–OH interfacial relationship and proposes a defect–engineered interfacial regulation strategy that integrates surface hydroxyl enrichment with N_v –guided Cu_2O interfacial stabilisation for designing efficient and stable carbon–nitride–based catalysts for HCO.

CRediT authorship contribution statement

Mingyue Li: Methodology, Investigation, Formal analysis, Data curation, Conceptualization. **Zhuang Guo:** Writing – review & editing, Methodology, Formal analysis. **Zhixiong Hu:** Formal analysis. **Dan Li:** Formal analysis. **Fang Chang:** Conceptualization. **Jian Wei:** Methodology. **Maosheng Zheng:** Writing – review & editing.

Declaration of competing interest

The authors declare that they have no known competing financial interests or personal relationships that could have appeared to influence the work reported in this paper.

Acknowledgements

This work was supported by the National Natural Science Foundation of China (Grant Nos. 52370038 and 22206177).

Appendix A. Supplementary data

Supplementary data to this article can be found online at https://doi.org/10.1016/j.cej.2026.180509.

Data availability

Data will be made available on request.

References

[1] J. Wang, H. Chen, Catalytic ozonation for water and wastewater treatment: Recent advances and perspective, Sci. Total Environ. 704 (2020) 135249, https://doi.org/10.1016/j.scitotenv.2019.135249.
[2] C.V. Rekhate, J.K. Srivastava, Recent advances in ozone-based advanced oxidation processes for treatment of wastewater- A review, Chem. Eng. J. Adv. 3 (2020) 100031, https://doi.org/10.1016/j.ceja.2020.100031.
[3] P. Kumari, A. Kumar, Advanced oxidation process: A remediation technique for organic and non-biodegradable pollutant, Results Surf. Interfaces 11 (2023) 100122, https://doi.org/10.1016/j.rsurfi.2023.100122.
[4] H. Wang, X. Lin, Y. Huang, W. Bian, L. Ma, Two advanced oxidation pathways of modified iron-shavings participation in ozonation, Sep. Purif. Technol. 244 (2020) 116838, https://doi.org/10.1016/j.seppur.2020.116838.
[5] T. Zhang, W. Li, J.P. Croué, Catalytic ozonation of oxalate with a cerium supported palladium oxide: An efficient degradation not relying on hydroxyl radical oxidation, Environ. Sci. Technol. 45 (2011) 9339–9346, https://doi.org/10.1021/es202209j.
[6] S. Gao, Z. Zhao, Y. Xu, J. Tian, H. Qi, W. Lin, F. Cui, Oxidation of sulfamethoxazole (SMX) by chlorine, ozone and permanganate—A comparative study, J. Hazard. Mater. 274 (2014) 258–269, https://doi.org/10.1016/j.jhazmat.2014.04.024.
[7] X. Li, L. Fu, F. Chen, S. Zhao, J. Zhu, C. Yin, Application of heterogeneous catalytic ozonation in wastewater treatment: an overview, Catalysts 13 (2023) 342, https://doi.org/10.3390/catal13020342.
[8] B. Wang, H. Zhang, F. Wang, X. Xiong, K. Tian, Y. Sun, T. Yu, Application of heterogeneous catalytic ozonation for refractory organics in wastewater, Catalysts 9 (2019) 241, https://doi.org/10.3390/catal9030241.
[9] D. Ma, Q. Lian, Y. Zhang, Y. Huang, X. Guan, Q. Liang, C. He, D. Xia, S. Liu, J. Yu, Catalytic ozonation mechanism over M_1-N_3C_1 active sites, Nat. Commun. 14 (2023) 7011, https://doi.org/10.1038/s41467-023-42853-8.
[10] W. Qu, S. Tang, Z. Tang, T. Zhong, H. Zhao, S. Tian, D. Shu, C. He, Refining asymmetric low-coordinated Fe-N_3 motif to boost catalytic ozonation activity, Adv. Funct. Mater. 34 (2024) 2314187, https://doi.org/10.1002/adfm.202314187.
[11] Y. Huang, D. Ma, W. Liu, D. Xia, L. Hu, J. Yang, P. Liao, C. He, Enhanced catalytic ozonation for eliminating CH_3SH via graphene-supported positively charged atomic Pt undergoing Pt^{2+}/Pt^{4+} redox cycle, Environ. Sci. Technol. 55 (2021) 16723–16734, https://doi.org/10.1021/acs.est.1c06938.
[12] Z. Gao, A. Li, X. Liu, M. Peng, S. Yu, M. Wang, Y. Ge, C. Li, T. Wang, Z. Wang, W. Zhou, D. Ma, Shielding Pt/γ-Mo_2N by inert nano-overlays enables stable H_2 production, Nature 638 (2025) 690–696, https://doi.org/10.1038/s41586-024-08483-w.
[13] P. Yang, J. Li, D.G. Vlachos, S. Caratzoulas, Tuning active site flexibility by defect engineering of graphene ribbon edge-hosted Fe−N_3 sites, Angew. Chem. Int. Ed. 63 (2024) e202311174, https://doi.org/10.1002/anie.202311174.
[14] Y. Wang, X. Duan, Y. Xie, H. Sun, S. Wang, Nanocarbon-based catalytic ozonation for aqueous oxidation: engineering defects for active sites and tunable reaction pathways, ACS Catal. 10 (2020) 13383–13414, https://doi.org/10.1021/acscatal.0c04232.
[15] W. Chen, H. He, J. Liang, X. Wei, X. Li, J. Wang, L. Li, A comprehensive review on metal based active sites and their interaction with O_3 during heterogeneous catalytic ozonation process:types, regulation and authentication, J. Hazard. Mater. 443 (2023) 130302, https://doi.org/10.1016/j.jhazmat.2022.130302.
[16] W.-D. Oh, V.W.C. Chang, Z.-T. Hu, R. Goei, T.-T. Lim, Enhancing the catalytic activity of g-C_3N_4 through Me doping (Me=Cu, Co and Fe) for selective sulfathiazole degradation via redox-based advanced oxidation process, Chem. Eng. J. 323 (2017) 260–269, https://doi.org/10.1016/j.cej.2017.04.107.
[17] F. Qi, J. Peng, Z. Liang, J. Guo, J. Liu, T. Fang, H. Mao, Strong metal-support interaction (SMSI) in environmental catalysis: mechanisms, application, regulation strategies, and breakthroughs, Environ. Sci. Ecotechnol. 22 (2024) 100443, https://doi.org/10.1016/j.ese.2024.100443.
[18] B. Song, Z. Zeng, G. Zeng, J. Gong, R. Xiao, S. Ye, M. Chen, C. Lai, P. Xu, X. Tang, Powerful combination of g-C_3N_4 and LDHs for enhanced photocatalytic performance: A review of strategy, synthesis, and applications, Adv. Colloid Interf. Sci. 272 (2019) 101999, https://doi.org/10.1016/j.cis.2019.101999.
[19] Y. Yang, Z. Zeng, G. Zeng, D. Huang, R. Xiao, C. Zhang, C. Zhou, W. Xiong, W. Wang, M. Cheng, W. Xue, H. Guo, X. Tang, D. He, Ti_3C_2 Mxene/porous g-C_3N_4 interfacial Schottky junction for boosting spatial charge separation in photocatalytic H_2O_2 production, Appl. Catal. B Environ. 258 (2019) 117956, https://doi.org/10.1016/j.apcatb.2019.117956.
[20] D. He, C. Zhang, G. Zeng, Y. Yang, D. Huang, L. Wang, H. Wang, A multifunctional platform by controlling of carbon nitride in the core-shell structure: from design to construction, and catalysis applications, Appl. Catal. B Environ. 258 (2019) 117957, https://doi.org/10.1016/j.apcatb.2019.117957.
[21] W. Wang, Q. Niu, G. Zeng, C. Zhang, D. Huang, B. Shao, C. Zhou, Y. Yang, Y. Liu, H. Guo, W. Xiong, L. Lei, S. Liu, H. Yi, S. Chen, X. Tang, 1D porous tubular g-C_3N_4 capture black phosphorus quantum dots as 1D/0D metal-free photocatalysts for oxytetracycline hydrochloride degradation and hexavalent chromium reduction, Appl. Catal. B Environ. 273 (2020) 119051, https://doi.org/10.1016/j.apcatb.2020.119051.
[22] C. Chen, N. Jia, K. Song, X. Zheng, Y. Lan, Y. Li, Sulfur-doped copper-yttrium bimetallic oxides: A novel and efficient ozonation catalyst for the degradation of aniline, Sep. Purif. Technol. 236 (2020) 116248, https://doi.org/10.1016/j.seppur.2019.116248.
[23] Y.f. Rao, H.j. Luo, C.h. Wei, L. Luo, Catalytic ozonation of phenol and oxalic acid with copper-loaded activated carbon, J. Cent. S. Univ. Technol. 17 (2010) 300–306, https://doi.org/10.1007/s11771-010-0046-y.
[24] Q. Gu, J. Rong, Y. Zhang, X. Zheng, Z. Zhou, Z. Li, S. Xu, Effective periodate activation of direct Z-scheme g-C_3N_4/Cu_2O heterojunction for photocatalytic norfloxacin degradation, anti-bacterial activity and toxicity assessment, Chem. Eng. J. 504 (2025) 159143, https://doi.org/10.1016/j.cej.2024.159143.
[25] J. Liu, J. Li, S. He, L. Sun, X. Yuan, D. Xia, Heterogeneous catalytic ozonation of oxalic acid with an effective catalyst based on copper oxide modified g-C_3N_4, Sep. Purif. Technol. 234 (2020) 116120, https://doi.org/10.1016/j.seppur.2019.116120.
[26] W. Wang, X. Sun, Z. Guo, Y. Liu, H. Shang, J. Ge, J. Wei, Y. Gao, Y. Song, Enhanced catalytic ozonation by O-doped g-C_3N_4/CuO: Synergistic multi-active sites for

broad pH applicability, Nano Res. 18 (2025) 94908079, https://doi.org/10.26599/NR.2025.94908079.
[27] S. Wang, D. Guo, M. Zong, C. Fan, X. Jun, D.-H. Wang, Unravelling the strong metal-support interaction between Ru quantum dots and g-C_3N_4 for visible-light photocatalytic nitrogen fixation, Appl. Catal. A Gen. 617 (2021) 118112, https://doi.org/10.1016/j.apcata.2021.118112.
[28] S. Yi, Z. Wang, Z. Wu, X. Yang, H. Wang, J. Yang, X. She, H. Xu, Monodispersed Cu sites assembled on ultrathin 2D C_3N_4 for efficient electrocatalytic CO_2 methanation, Appl. Surf. Sci. 681 (2025) 161492, https://doi.org/10.1016/j.apsusc.2024.161492.
[29] S. Wang, L. Wang, W. Liu, C. Ke, M. Li, J. Hui, Recent progress in intrinsic defect modulation of g-C_3N_4 based materials and their photocatalytic properties, Nano Res. 18 (2025) 94907125, https://doi.org/10.26599/NR.2025.94907125.
[30] T. Ren, K. Lu, F. Tao, H. Ren, N. Yan, J. Miao, X. Huang, X. Zhang, Phosphorus-induced single-atom iron coordination symmetry disruption for superior catalytic ozonation, Nat. Commun. 16 (2025) 9037, https://doi.org/10.1038/s41467-025-64099-2.
[31] S.P. J. John, T.P.D. Rajan, G.M. Anilkumar, T. Yamaguchi, S.C. Pillai, U.S. Hareesh, Graphitic carbon nitride (g-C_3N_4) based heterogeneous single atom catalysts: synthesis, characterisation and catalytic applications, J. Mater. Chem. A 11 (2023) 8599–8646, https://doi.org/10.1039/D2TA09776A.
[32] V. Nguyen, B.D. Etz, S. Pylypenko, S. Vyas, Periodic trends behind the stability of metal catalysts supported on graphene with graphitic nitrogen defects, ACS Omega 6 (2021) 28215–28228, https://doi.org/10.1021/acsomega.1c04306.
[33] D. Zaoralova, R. Langer, M. Otyepka, Iron single-atom catalysts anchored on defect-engineered N-doped graphene reveal an interplay between CO_2 reduction activity and stability, ACS Sustain. Chem. Eng. 13 (2025) 8319–8330, https://doi.org/10.1021/acssuschemeng.5c01417.
[34] X. Xu, Y. Xu, Y. Liang, H. Long, D. Chen, H. Hu, J.Z. Ou, Vacancy-modified g-C_3N_4 and its photocatalytic applications, Mater. Chem. Front. 6 (2022) 3143–3173, https://doi.org/10.1039/D2QM00604A.
[35] K. Edalati, R. Uehiro, S. Takechi, Q. Wang, M. Arita, M. Watanabe, T. Ishihara, Z. Horita, Enhanced photocatalytic hydrogen production on GaN–ZnO oxynitride by introduction of strain-induced nitrogen vacancy complexes, Acta Mater. 185 (2020) 149–156, https://doi.org/10.1016/j.actamat.2019.12.007.
[36] C. Ji, S.-N. Yin, S. Sun, S. Yang, An in situ mediator-free route to fabricate Cu_2O/g-C_3N_4 type-II heterojunctions for enhanced visible-light photocatalytic H_2 generation, Appl. Surf. Sci. 434 (2018) 1224–1231, https://doi.org/10.1016/j.apsusc.2017.11.233.
[37] Y. Liu, Z. Song, W. Wang, Z. Wang, Y. Zhang, C. Liu, Y. Wang, A. Li, B. Xu, F. Qi, A $CuMn_2O_4$/g-C_3N_4 catalytic ozonation membrane reactor used for water purification: Membrane fabrication and performance evaluation, Sep. Purif. Technol. 265 (2021) 118268, https://doi.org/10.1016/j.seppur.2020.118268.
[38] L. Zhong, M. Ying, Z. Mou, R. Luo, J. Sun, D. Liu, W. Lei, Template-free preparation of carbon nitride hollow spheres with adjustable sizes for photocatalytic hydrogen generation, J. Colloid Interface Sci. 612 (2022) 479–487, https://doi.org/10.1016/j.jcis.2021.12.154.
[39] Y. Zhang, Q. Li, Y. Long, J. Zou, Z. Song, C. Liu, L. Liu, F. Qi, B. Xu, Z. Chen, Catalytic ozonation benefit from the enhancement of electron transfer by the coupling of g-C_3N_4 and $LaCoO_3$: discussion on catalyst fabrication and electron transfer pathway, Appl. Catal. B Environ. 254 (2019) 569–579, https://doi.org/10.1016/j.apcatb.2019.05.019.
[40] J. Ma, Q. Yang, Y. Wen, W. Liu, Fe-g-C_3N_4/graphitized mesoporous carbon composite as an effective Fenton-like catalyst in a wide pH range, Appl. Catal. B Environ. 201 (2017) 232–240, https://doi.org/10.1016/j.apcatb.2016.08.048.
[41] V.K. Parida, R. Dhakad, S. Chowdhury, A.K. Gupta, Facile synthesis of a 2D/3D Z-scheme Cu-g-C_3N_4/BiOBr heterojunction for enhanced photocatalytic degradation of ciprofloxacin under visible light irradiation, J. Environ. Chem. Eng. 11 (2023) 111569, https://doi.org/10.1016/j.jece.2023.111569.
[42] T.T. Nguyen, K. Edalati, Synergistic interface and oxygen/nitrogen vacancy engineering in g-C_3N_4/Cu_2O under high pressure for efficient CO_2 photoreduction, J. Colloid Interface Sci. 702 (2026) 138951, https://doi.org/10.1016/j.jcis.2025.138951.
[43] X.-H. Li, J. Zhang, X. Chen, A. Fischer, A. Thomas, M. Antonietti, X. Wang, Condensed graphitic carbon nitride nanorods by nanoconfinement: promotion of crystallinity on photocatalytic conversion, Chem. Mater. 23 (2011) 4344–4348, https://doi.org/10.1021/cm201688v.
[44] T. Ma, Q. Shen, B.Z.J. Xue, R. Guan, X. Liu, H. Jia, B. Xu, Facile synthesis of Fe-doped g-C_3N_4 for enhanced visible-light photocatalytic activity, Inorg. Chem. Commun. 107 (2019) 107451, https://doi.org/10.1016/j.inoche.2019.107451.
[45] A. Svidrytski, D. Hlushkou, M. Thommes, P.A. Monson, U. Tallarek, Modeling the impact of mesoporous silica microstructures on the adsorption hysteresis loop, J. Phys. Chem. C 124 (2020) 21646–21655, https://doi.org/10.1021/acs.jpcc.0c07571.
[46] J.R. Zhang, Y. Ma, S.Y. Wang, J. Ding, B. Gao, E. Kan, W. Hua, Accurate K-edge X-ray photoelectron and absorption spectra of g-C_3N_4 nanosheets by first-principles simulations and reinterpretations, Phys. Chem. Chem. Phys. 21 (2019) 22819–22830, https://doi.org/10.1039/C9CP04573B.
[47] D.J. Morgan, Core-level reference spectra for bulk graphitic carbon nitride (g-C_3N_4), Surf. Sci. Spectra 28 (2021) 014007, https://doi.org/10.1116/6.0001083.
[48] D. Liang, R. Shan, J. Gu, S. Wang, L. Cheng, H. Yuan, Y. Chen, Unraveling the impact of three coordinate nitrogen (N_{3c}) vacancies in porous carbon nitride nanobelt for boosted photocatalytic degradation of microplastics and antibiotics, Appl. Catal. B Environ. Energy 358 (2024) 124402, https://doi.org/10.1016/j.apcatb.2024.124402.
[49] Q. Zhang, L. Li, Q. Zhou, H. Zhang, H. Zhang, B. An, H. Ning, T. Xing, M. Wang, M. Wu, W. Wu, Boosting C_3H_6 epoxidation via tandem photocatalytic H_2O_2 production over nitrogen-vacancy carbon nitride, ACS Catal. 13 (2023) 13101–13110, https://doi.org/10.1021/acscatal.3c02904.
[50] M. Liu, J. Liu, Z. Zeng, X. Wang, J. Jia, X. Gu, Z. Zheng, Steric hindrance effect induced photopurification of styrene oxide over surface modified polymeric carbon nitride, Sep. Purif. Technol. 300 (2022) 121929, https://doi.org/10.1016/j.seppur.2022.121929.
[51] M.S. Azami, K. Ismail, M.A.M. Ishak, A. Zuliahani, S.R. Hamzah, W.I. Nawawi, Formation of an amorphous carbon nitride/titania composite for photocatalytic degradation of RR4 dye, J. Water Process Eng. 35 (2020) 101209, https://doi.org/10.1016/j.jwpe.2020.101209.
[52] K. Avasthi, A. Bohre, J. Teržan, I. Jerman, J. Kovač, B. Likozar, Single step production of styrene from benzene by alkenylation over palladium-anchored thermal defect rich graphitic carbon nitride catalyst, Mol. Catal. 514 (2021) 111844, https://doi.org/10.1016/j.mcat.2021.111844.
[53] M.R. Rizk, M.G. Abd El-Moghny, Controlled galvanic decoration boosting catalysis: Enhanced glycerol electro-oxidation at Cu/Ni modified macroporous films, Int. J. Hydrog. Energy 46 (2021) 645–655, https://doi.org/10.1016/j.ijhydene.2020.10.004.
[54] F. Guy, H. Runtti, L. Duclaux, M. Ondarts, L. Reinert, J. Outin, E. Gonze, S. Bonnamy, Y. Soneda, Synthesis and characterization of Cu doped activated carbon beads from chitosan, Microporous Mesoporous Mater. 322 (2021) 111147, https://doi.org/10.1016/j.micromeso.2021.111147.
[55] M. Soldemo, F. Garcia-Martinez, C.M. Goodwin, P. Lömker, M. Shipilin, A. Nilsson, P. Amann, S. Kaya, J. Weissenrieder, Using Auger transitions as a route to determine the oxidation state of copper in high-pressure electron spectroscopy, Surf. Sci. 749 (2024) 122565, https://doi.org/10.1016/j.susc.2024.122565.
[56] T. Yano, M. Ebizuka, S. Shibata, M. Yamane, Anomalous chemical shifts of Cu 2p and Cu LMM Auger spectra of silicate glasses, J. Electron Spectrosc. Relat. Phenom. 131-132 (2003) 133–144, https://doi.org/10.1016/S0368-2048(03)00126-9.
[57] R. Vijayarangan, A.K. Purayil, S. Mohan, R. Ilangovan, Neem extract-mediated green reduction of Ag, Cu, and Fe onto g-C_3N_4 photocatalysts for LED-light-driven multipollutant degradation and H_2 generation, J. Water Process Eng. 87 (2026) 110077, https://doi.org/10.1016/j.jwpe.2026.110077.
[58] Y. Xue, B. Zhou, Y. Chen, J. Wang, L. Yang, Q. Zhou, W. Lan, S. Fang, Hydroxyl-rich g-C_3N_4 supported copper-cobalt oxide nano-fenton-like catalyst for aromatic pollution removal from aqueous solutions, Process Saf. Environ. Prot. 207 (2026) 108434, https://doi.org/10.1016/j.psep.2026.108434.
[59] W.K. Wang, H.M. Zhang, S.B. Zhang, Y.Y. Liu, G.Z. Wang, C.H. Sun, H.J. Zhao, Potassium ion assisted regeneration of active cyano groups in carbon nitride nanoribbons: visible light driven photocatalytic nitrogen reduction, Angew. Chem. Int. Ed. 58 (2019) 16644–16650, https://doi.org/10.1002/anie.201908640.
[60] Z. Song, M. Wang, Z. Wang, Y. Wang, R. Li, Y. Zhang, C. Liu, Y. Liu, B. Xu, F. Qi, Insights into heteroatom-doped graphene for catalytic ozonation: active centers, reactive oxygen species evolution, and catalytic mechanism, Environ. Sci. Technol. 53 (2019) 5337–5348, https://doi.org/10.1021/acs.est.9b01361.
[61] F.J. F.J.R Beltrán, L.A. Fernández, P.M. Álvarez, R. Montero-de-Espinosa, Kinetics of catalytic ozonation of oxalic acid in water with activated carbon, Ind. Eng. Chem. Res. 41 (2002) 6510–6517, https://doi.org/10.1021/ie020311d.
[62] S.H. J.J.C. Wu, M. Muruganandham, Catalytic ozonation of oxalic acid using carbon-free rice husk ash catalysts, Ind. Eng. Chem. Res. 47 (2008) 2919–2925, https://doi.org/10.1021/ie071093x.
[63] Y. Huang, Y. Sun, Z. Xu, M. Luo, C. Zhu, L. Li, Removal of aqueous oxalic acid by heterogeneous catalytic ozonation with MnO_x/sewage sludge-derived activated carbon as catalysts, Sci. Total Environ. 575 (2017) 50–57, https://doi.org/10.1016/j.scitotenv.2016.10.026.
[64] U. von Gunten, Ozonation of drinking water: part I. Oxidation kinetics and product formation, Water Res. 37 (2003) 1443–1467, https://doi.org/10.1016/S0043-1354(02)00457-8.
[65] T. Fotiou, T.M. Triantis, T. Kaloudis, K.E. O'Shea, D.D. Dionysiou, A. Hiskia, Assessment of the roles of reactive oxygen species in the UV and visible light photocatalytic degradation of cyanotoxins and water taste and odor compounds using C-TiO_2, Water Res. 90 (2016) 52–61, https://doi.org/10.1016/j.watres.2015.12.006.